J. Quant. Spectrosc. Radiat. Transfer Vol. 48, No. 5/6, pp. 629–643, 1992
Printed in Great Britain

0022-4073/92 $5.00 + 0.00
Pergamon Press Ltd

ATMOSPHERIC 60-GHz OXYGEN SPECTRUM: NEW LABORATORY MEASUREMENTS AND LINE PARAMETERS

H. J. LIEBE,† P. W. ROSENKRANZ,‡ and G. A. HUFFORD†

†National Telecommunications and Information Administration, Institute for Telecommunication Sciences, Boulder, CO 80303 and ‡Research Laboratory of Electronics, Massachusetts Institute of Technology, Cambridge, MA 02139, U.S.A.

(Received 16 March 1992)

Abstract—Over 5000 absolute absorption values for pressure-broadened O_2 lines in dry air were measured at frequencies from 49 to 67 GHz in 0.1-GHz-increments. The controlled laboratory studies were carried out at three temperatures (6, 30, and 54°C) for 11 pressure values ranging between 1.3 and 101 kPa. The spectrometer consisted of a Fabry–Pérot resonator combined with an automatic network analyzer. The detection sensitivity was better than ± 0.02 dB/km, and measurement uncertainties were estimated to be typically better than ± 0.05 dB/km for attenuation rates below 3 dB/km, or better than $\pm 2\%$ for higher rates. The extensive data set was compared with predictions by an established model (MPM89). Systematic discrepancies were recognized and reduced by means of a readjustment of line parameters. The new model (MPM92) is given here.

1. INTRODUCTION

For the frequency range from 50 to 70 GHz, molecular oxygen is the prime absorber of the gaseous atmosphere between sea level and 90 km altitude. This absorption results from magnetic-dipole transitions in which the unpaired electron spin of the $^3\Sigma_g$ electronic ground state changes alignment with respect to the rotational angular momentum of the molecule. In 1947, VanVleck[1] published the first definitive theory to describe the O_2 spectrum in air. Since the earlier laboratory[2,3] and field[4,5] studies, the problem has continued to captivate the interest of experimental[6–14] and theoretical[15–27] research.

Collisional broadening due to increasing pressure causes the lines to blend together so that at 1 atm (101 kPa) an unstructured, composite shape spreads about ± 10 GHz around a common 60-GHz center. Because of line mixing (overlap interference), the resulting intensity is not the simple sum of isolated line responses. At pressures below 20 kPa, over 30 discernible, pressure-broadened lines appear. For pressures smaller than 1 kPa (mesospheric region), the line properties are controlled by the geomagnetic Zeeman effect.[26,27]

Knowledge of the transmission rates for radiation relies on accurate modeling of the spectral O_2 behavior. This information is important to applications in communication[30,31] and remote sensing;[32–34] it also provides a means for validating theoretical calculations[22–25] based on intermolecular potential functions. The highly frequency-selective spectral properties need to be corroborated by controlled laboratory studies, where gas composition ($O_2 + N_2$, Ar, H_2O), frequency, pressure, and temperature provide the known variables. The commonly-used theoretical expressions for microwave absorption by oxygen in atmospheric air[25,29] have incorporated more than 250 spectroscopic coefficients that were derived from laboratory measurements.[6,9]

The paper deals with experimental and analytical results obtained during a detailed study of the 60-GHz O_2 absorption in $O_2 + N_2$ mixtures. Section 2 addresses the measurement principle of the spectrometer and operational procedures; Sec. 3 deals with attributes of the extensive data set made up by over 5000 absolute absorption values;[12] and Sec. 4 formulates the dry-air part of the prediction model MPM[29] and discusses model adjustments to line mixing parameters that reduce the residuals between measured and predicted data for pressures in the 10–101 kPa range.

2. EXPERIMENTAL DETAILS

2.1. Measurement principle

Spectroscopic properties of gas are conveniently expressed by a complex refractivity,

$$\mathbf{N} = N' + iN'' = (\mathbf{n} - 1)10^6 \quad \text{(ppm)}, \tag{1}$$

where $\mathbf{n}$ is the complex refractive index of the medium. The measurements described here used a resonance spectrometer[10,12] to measure $\mathbf{N}$, especially the imaginary part N''. The power attenuation rate α follows from (frequency f in GHz)

$$\alpha = 0.1820 f N'' \quad \text{(dB/km)}. \tag{2}$$

The spectrometer performance (sensitivity, stability, etc.) was much improved over past efforts[14,10] by state-of-the-art millimeter-wave instrumentation. Two key components of our experimental setup were a Fabry–Pérot resonator cell and an automatic network analyzer. Precision measurements were conducted by analysing both amplitude and phase of the resonance signal. Interactive spectrometer operations, automatic recordings, and data reduction to attenuation rates were handled by a microcomputer.[12]

2.2. Resonator characteristics

A semiconfocal, one-port Fabry-Pérot resonator was the heart of the spectrometer. A flat and a spherical (40 cm radius of curvature) mirror were separated a distance d by three invar rods. Both mirrors were made of silver-plated brass with optically polished surfaces; their diameter was 10 cm. The structure was housed in a stainless steel vacuum chamber that was temperature-controlled.[35] Resonances were excited via a circular coupling iris centered in the flat mirror, followed by a quartz glass vacuum window and V-band waveguide. Fundamental $\mathrm{TEM}_{0,0,q}$ modes were utilised, for which the center frequencies are calculated by means of[36]

$$f_r = \frac{c}{n'}\frac{(4q+1)}{8d} \quad \text{(GHz)}, \tag{3}$$

where $c = 299.792$ (mm × GHz) is the speed of light in vacuum; q is the number of half-wavelength nodes between the mirrors; and n' is the real part of the refractive index of the test gas [Eq. (1)]. Resonance frequencies change due to refractive tuning by the gas, $f_r = f_0/n'$. The mirror spacing, $d = 205 \pm 12$ mm, was varied with a precision ($\Delta d = \pm 0.5\ \mu$m) micrometer (e.g., $f_0 = 62.500$ GHz, when $d = 204.458$ mm, $q = 85$, and $n' = 1$ for $P_0 = 0$). Mechanical tuning reproduced f_r to within $\pm$ 75 kHz. Between 49 and 66 GHz, the vacuum-halfwidths B_0 of $\mathrm{TEM}_{0,0,q}$ modes were found to be nearly constant ($\approx$105 kHz). The key parameter for a high detection sensitivity is the effective path length $L_E = c/4\pi B_0 = 23.86/B_0 \approx 0.24$ km.

2.2.1. Properties of the detected signal. An automatic network analyzer (ANA) was employed, capable of making vector (magnitude and phase) measurements of a reflected signal with unprecedented speed, accuracy, and convenience. A synthesised source generator (10–15 GHz) followed by a 5× multiplier (50–75 GHz) provided the RF stimulus for the resonator. The RF signal was centered at f_r and changed frequency in discrete steps over a band Δf which covered several halfwidths B. Reflected and incident signals were linearly detected and processed into a normalised amplitude ratio called complex reflection scattering parameter $\mathbf{S}_{11}$. The first step in the detection process was the normalisation of the baseline signal level to $\mathbf{S}_{11}^0 = -1 + i0$ over the frequency span Δf. A "response" calibration (ANA feature) with a short provided the reference. The waveguide plane of the coupling iris acted as the short when, under computer control, the resonance was defeated with a motor-driven metal vane that rotated into the space of the resonance field. The calibrated $\mathbf{S}_{11}$ output, a sample of which is shown in Fig. 1, reveals the quintessence of the experiment.

The resonance centered at f_r may be described by three interrelated quality values, $Q^{-1} = Q_u^{-1} + Q_c^{-1}$, where Q, Q_u, and Q_c refer to loaded, unloaded, and coupling Q-values, respectively. For weak coupling and high Q-values ($Q_c > Q > 10^5$), the reflected signal follows a Lorentzian resonance behavior,[37]

$$\mathbf{S}_{11}(f) = s' + is'' + a[1 + i(f - f_r)/B]^{-1}, \tag{4}$$

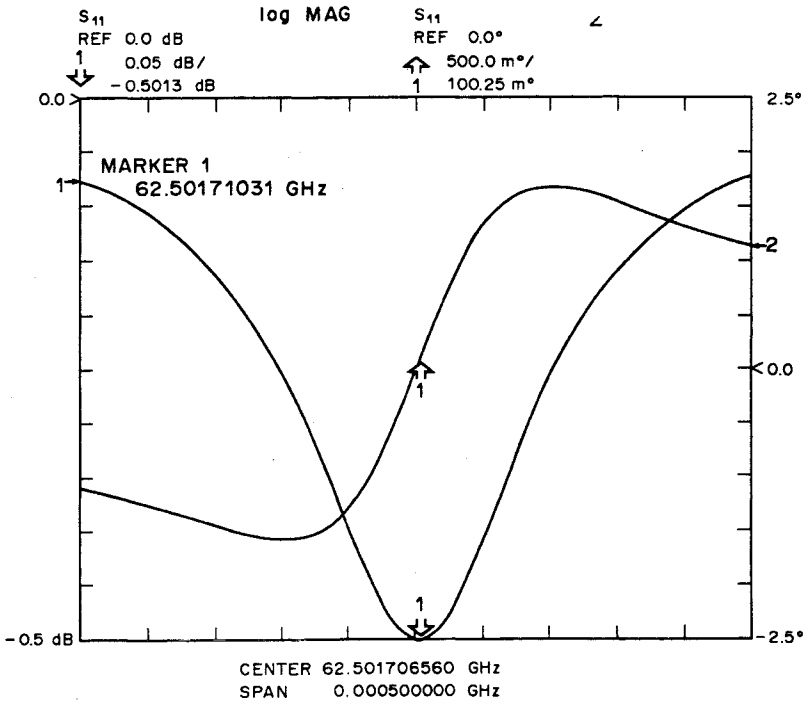

Fig. 1. ANA display of complex reflection scattering coefficient $S_{11}(f_0 \pm 250\,\text{kHz})$ for a resonance at $f_0 = 62.5017\,\text{GHz}$ with the halfwidth, $B_0 = 104\,\text{kHz}$, in units of log magnitude (dB) and phase angle (deg + 180°). Experimental conditions: $P_0 = 0$, $T = 30°\text{C}$; $Q = 2.998(4) \times 10^5$, $Q_u = 3.176(4) \times 10^5$ ($A = 5.82\,\text{kHz}$, $g_0 = 17.9$).

where $a = 1 - Q/Q_u = Q/Q_c$ is the reflection dip at the center frequency f_r and $B = f_r/2Q$ the halfwidth of the resonance. A statistical analysis of S_{11} data with the method of least squares provided a means to extract the parameters s', s'', f_r, a, and B. We found that a and B were strongly coupled (correlation coefficient was >0.9). Hence, the alternate functional form introduced was

$$S_{11}(f) = s' + is'' + [g + i(f - f_r)/A]^{-1}, \tag{5}$$

where $g = a^{-1}$ is an amplitude factor, and $A = aB = f_r/2Q_c$ is the invariable resonance strength. The parameters g and A were found to be nearly independent (correlation coefficient was <0.3), and making Eq. (5) the better choice to extract s', s'', f_r, g, and A.

The spectrometer measures (from changes in the resonance signal S_{11}) the complex refractivity [Eq. (1)],

$$N = [(f_0 - f_r) + iA(g_p - g_0)](10^6/f_r) \quad \text{(ppm)}. \tag{6}$$

When air (P) is introduced into the evacuated (P_0) chamber, the center frequency shifts to lower values ($f_0 \rightarrow f_r$) and the resonance dip decreases ($g_0 \rightarrow g_p$). Parameters subscripted by 0 refer to the reference state P_0. The attenuation rate, Eq. (2), is (A in kHz)

$$\alpha = 0.1820A(g_p - g_0) \quad \text{(dB/km)}. \tag{7}$$

Experiments were conducted with $[A, g_0]$-combinations, which varied from weak [0.73, 141] to strong [7.7, 13.4] resonance signals. The term $A(g_p - g_0)$ must be resolved to about 0.1 kHz to obtain a measurement precision of ± 0.02 dB/km; that required magnitude and phase changes of the signal S_{11} to be detected to better than 2×10^{-3} and 40 millidegrees, respectively.

2.3. Test air

Absorption by synthetic air was studied. The supplier of the laboratory-grade gas mixture certified its composition and impurities as follows: $20.45 \pm 0.02\%$ O_2 (99.519% $^{16}O^{16}O$; 0.407% $^{16}O^{18}O$; 0.074% $^{16}O^{17}O$, ... relative abundances), 79.55% N_2, 2.1 ppm H_2O, $\leqslant 1$ ppm CO_2,

and $\leqslant 0.1$ ppm total hydrocarbon content. The *test air* thus contained slightly less O_2 than the natural abundance of 20.946%.[38] This deficiency of O_2 was taken into account in the factor

$$\xi = 0.2045/0.20946 = 0.9763, \tag{8}$$

which was introduced into the model used for comparison with the measurements (Sec. 4). The *test air* also contained less Ar, CO_2, and H_2O than natural air. Although the first two are not sufficiently abundant to cause significant changes to the dry air model, the variable amount of water vapor in the atmosphere needs to be formally considered. Barometric pressure is expressed by $P = p + e$ (kPa), where p and e ($=0$ here) are the partial pressures of dry air and water vapor, respectively.

Total pressure P was measured by a differential capacitance manometer ($\pm 0.2\%$) and its calibration periodically checked against a precision ($\pm 0.2\%$) quartz Bourdon-type manometer. Pressure changes were controlled by a piezoelectric leak valve. To ensure quasi-static gas conditions, the pressure was varied between 0 and 101 kPa at rates smaller than ± 10 kPa/min. A reference vacuum was provided by a two-stage rotary vane pump (750 l/min) preceded by a zeolith trap. The cell could be evacuated to ultimate pressures, $P_0 \leqslant 0.03$ Pa.

2.4. Operational details

Spectrometer operations were computer-controlled. A microcomputer was run by BASIC software, offering menus for single and multiple resonance scanning. The S-parameters were measured over the span Δf at 51 frequency points, each being averaged 128 times. The frequency span was set at $\Delta f = 500$ kHz and centered automatically at f_r. The signal was acquired in $t_s = 2$ sec by stepping in 10 kHz increments.

The complex ANA signal output $S_{11}(f)$ was fitted to the function provided by Eq. (5) by means of a fast, non-linear least-square (NLS) routine based on the iterative Levenberg–Marquardt algorithm.[39] The NLS-fit was performed in two steps.[12] The first step revealed s', s'', f_r, g_p, and A; the final fit to f_r and g_p was initialised by the three remaining, invariant parameters. One attenutation value (α) is established by two S_{11} data sets, and its uncertainty was computed from the statistics of 10 repetitions.

2.4.1. Multiple resonance operation. The resonator supported a comb of $TEM_{0,0,q}$ resonances presented by Eq. (3) which appeared in $c/2d$ intervals (e.g., 0.733 GHz for $d = 204.5$ mm) with Q-factors, $Q \approx (2.5\text{–}3.5)10^5$. At computer-selected frequencies f_r, each measurement sequence was repeated 10 times before increasing the pressure. Eleven pressure values were preprogrammed, in addition to initial and final records at $P_0 = 0$. Data runs above 60 GHz utilised five successive resonances and took about 1 h; below 60 GHz, a measurement sequence contained 15 resonances and took about 4 h.

2.4.2. Measurement example. The operational rationale and typical uncertainties of the spectrometer parameters (standard deviations from the mean in terms of the final listed digits are given in parentheses) are demonstrated by an example. The resonator was tuned to $f_0 = 55.7$ GHz ($q = 75$) at $T = 30$°C and 10 sets of S_{11} data were taken. The NLS-fit yielded the following data: for baseline calibration, $s' = -0.99952(5)$ and $s'' = 0.0002(1)$; for resonance strength, $A = 1.267(5)$ (kHz); for center frequency and amplitude factor at the initial pressure $P_0 = 0$, $f_0 = 55{,}672{,}046.2(3)$ (kHz) and $g_0 = 83.9(1)$; the same at $P = 101.3$ (kPa), $f_r = 55{,}657{,}524.4(4)$ (kHz) and $g_p = 106.8(2)$; and at the final pressure $P_0 = 0$, $f_0 = 55{,}672{,}034.4(2)$ (kHz) and $g_0 = 84.0(1)$; for the vacuum attenuation rate, $\alpha_0(P_0) = 0.02(4)$, and for *test air*, $\alpha(P) = 5.27(5)$ (dB/km).

2.5. Sensitivity and longterm stability

The S_{11} data were detected with a precision equal to 3×10^{-5} (16-bit A/D converter, including sign) at a noise level, $\delta S_{11} \approx 3 \times 10^{-4}$. Measuring small differences between two calibrated envelope responses fitted by Eq. (5) proved to be the main challenge for optimising the spectrometer. Precise temperature control and a solid resonator construction were mandatory to ensure a drift-free value for f_r. Typically, the detection scheme allowed about 200 Hz frequency resolution, which implies taxing requirements for the mechanical integrity of the resonator structure. For example, the spacing d has to remain stable to within ± 0.7 nm (!) over the time period of a measurement sequence (1–5 h).

Table 1. r.m.s. error σ [$\pm$(dB/km) $\times 10^3$] of the residuals $\Delta\alpha$ for data groups $\alpha(n \times f_r)_{P,T}$, obtained from fits with MPM89 and MPM92 (see Fig. 2).

		6°C		30°C		54°C	
Pressure	Data	MPM89	MPM92	MPM89	MPM92	MPM89	MPM92
P, kPa	n†	σ					
0	190	61	61	58	58	49	49
1.21	107	42	42 (39)‡	55	55 (53)‡	66	66 (63)‡
1.90	117	51	51 (48)	65	65 (60)	72	72 (71)
2.98	141	58	58 (54)	70	70 (67)	43	43 (39)
4.75	150	66	66 (62)	71	70 (69)	63	63 (60)
7.60	166	80	79 (71)	67	66 (64)	63	62 (58)
12.11	172	82	82 (71)	88	87 (81)	82	81 (74)
19.49	176	91	84 (80)	98	93 (88)	91	90 (86)
30.81	176	87	77 (76)	88	85 (83)	97	89 (84)
47.19	179	126	94 (95)	123	116(111)	117	107(102)
70.11	183	221	145(143)	185	150(144)	177	135(131)
101.3	190	262	229(194)	276	210(187)	240	168(150)

† Minimum number of points per data group (at 6 and 30°C there were 12 additional points available).

‡ RMS errors σ in parentheses were computed by assuming $\gamma_k^* = 1.05\,\gamma_k$ [see remarks below Eq. (17)] and $Y_k^* = 1.15\,Y_k$ [Eq. (27)].

The temperature of the insulated spectrometer cell was kept stable to ± 0.05°C by a proportional controller. Ambient temperature fluctuated typically by ± 3°C, while the long-term temperature stability of the cell remained at better than ± 0.2°C/day. The thermal time constant (~ 50 min/°C) of the resonator structure assured a short-term stability of about ± 0.01°C/min. At a thermal tuning rate of about 40 kHz/°C (at 60 GHz), millidegree changes were sufficient to shift f_r noticeably ($\geqslant 100$ Hz). To first order, however, attenuation rates α [Eq. (7)] are not affected by slight changes of f_r.

3. ATTENUATION RESULTS AND ERROR DISCUSSION

3.1. Residual errors

Attenuation rates α were measured from 49.2 to 67.3 GHz in 100 MHz increments ($f_r \times n$) at 11 pressures ($P = 1.2$–101 kPa) for three temperature groups ($T = 6$, 30, and 54°C). Tables listing data between 54 and 66 GHz have been published.[12] Two models for α_M (f, P, T) were employed to compute the residuals

$$\Delta\alpha = \alpha - \alpha_M. \tag{9}$$

The r.m.s. error σ of all (n) $\Delta\alpha_n$ for each P–T group serves to show how well the data fit the model. Results for σ are summarized in Table 1 for both the MPM89[29] and the MPM92 (Sec. 4) models and plotted in Fig. 2.

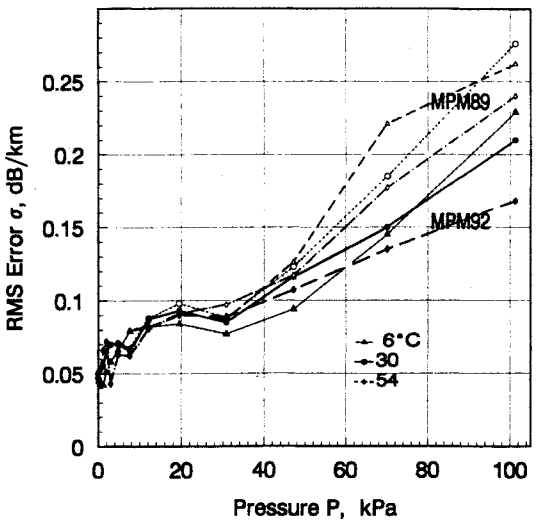

Fig. 2. Errors in fitting the attenuation measurements over the frequency range from 49 to 67 GHz with MPM89 and MPM92 (see Table 1).

3.2. *Random and systematic errors*

Experimental errors are normally separated into random and systematic components. A laboratory experiment offers the advantages of minimising random and averting systematic errors. Random errors originate from residual noise inherent in the measurement process, which distributes successive data in a normal (Gaussian) sense about some mean. In the absence of systematic errors, this mean approaches the true value as the number of independent measurements increases. Averaging the results of repeat measurements reduced noise influences during the acquisition period t_s (2 sec) that were caused by signal fluctuations δS_{11}. The number of repeat runs was limited to 10 due to the available capacity for data storage and the acquisition time for a measurement sequence.

Systematic errors cause a bias in the result, which (a) may be correctable, (b) remain uncorrected but can be included in the uncertainty statement, or in the worst case, (c) go undetected but unknowingly affect the measurement. Measurement uncertainties of the experimental variables f, P, and T, contributed only negligible errors to the measured attenuation rate; however, changing pressure loads the structure, introduces temperature gradients, and bends the vacuum window inside the coupling waveguide. Pressure behavior was tested at 10 frequencies between 58 and 66 GHz by performing data runs (0–110 kPa) with nitrogen as a non-absorbing substitute for air. Overall, attenuation readings were smaller than ± 0.1 dB/km. The pressure loading effect upon f_r was estimated to be about -2.5 Hz/kPa which, even at 101 kPa, does not affect the α recordings.

After completing the experiments with *test air*, a raw data base of over 6000 attenuation values was available. A few data series were found corrupted by various experimental problems, leaving about 5400 $\alpha(f_r, P, T)$ values of worthwhile data. One filter for data rejection was an MPM89-prediction[29] with $\pm 30\%$ tolerance bounds; another filter was the baseline behavior α_0. Data groups $\alpha(f_r \times n)_{P,T}$ for which the associated α_0 deviated from zero by more than ± 0.25 dB/km were rejected.

3.2.1. Baseline behavior. Under vacuum (P_0), a nearly perfect baseline, $\alpha_0 = 0.00 \pm 0.025$ dB/km, was registered over a 24-h period for data repeated in 1-min intervals. However, each measurement series stepped through a pressure sequence that began and ended with P_0. The value $\alpha_0(P_0)$ unmasked systematic errors that had occurred during the course of the series. For a temperature group, the distribution of individual standard deviations $0 \pm \Delta\alpha_0$ was random with the r.m.s. error σ given in Table 1. Data points $\alpha(f_r)_{P,T}$ were evaluated against their baseline values α_0.

4. THEORETICAL MODEL

A comprehensive millimeter-wave propagation model (MPM) has been developed by Liebe.[28,29] This algorithm predicts the atmospheric propagation characteristics of attenuation and delay over

a specific path by relating them to meterological variables such as pressure, temperature, humidity, suspended droplet concentration, and rainfall rate. Here we summarise the equations defining the dry air component of the MPM, and discuss revisions in the spectroscopic coefficients that have been prompted by the measurements described above.

4.1. The pressure-broadened O_2 microwave spectrum of air

The complex refractivity of dry air is predicted by

$$\mathbf{N}_M = N(0) + S_0\mathbf{F}_0(f) + \Sigma_k S_k \mathbf{F}_k(f) \quad \text{(ppm)}, \tag{10}$$

where $N(0) = 2.588p\theta$ represents the real and positive nondispersive refractivity. Here, the indices 0 and k identify nonresonant and line contributions, $S_{0,k}$ are intensity factors, $\mathbf{F}_{0,k}$ are complex spectral shape functions, p is the partial pressure of dry air, and $\theta = 300/T$ (T in Kelvin) is a relative, inverse temperature variable. The imaginary part, $\text{Im}\,\mathbf{N}_M = N''$, determines the predicted attenuation rate α_M [Eq. (2)].

4.1.1. Nonresonant spectrum. A small refractivity of dry air is due to the relaxation (Debye) spectrum of oxygen's magnetic dipole moment. The complex shape function is

$$\mathbf{F}_0(f) = -\frac{f}{f + i\gamma_0}. \tag{11}$$

Nonresonant absorption [imaginary part of Eq. (11)] is modeled by[29]

$$N_0'' = S_0 F_0'' = 6.14 \times 10^{-4} \xi p \theta^2 F_0'' \quad \text{(ppm)}, \tag{12}$$

where the shape function is $F_0'' = [(f/\gamma_0) + (\gamma_0/f)]^{-1}$, the width parameter is given by $\gamma_0 = 0.56 \times 10^{-2} P\,\theta^{0.8}$ (GHz), and the factor ξ [Eq. (8)] equals unity for natural air.

4.1.2. Line spectrum. Refractivity of dry air in the 50–70 GHz band is dominated by a resonant spectrum of oxygen, principally by 43 lines centered below 70 GHz and seven additional lines that extend the frequency range of the model to 1000 GHz. The individual line strength is represented by

$$S_k = a_1 \times 10^{-6} \xi p \theta^3 \exp[a_2(1-\theta)] \quad \text{(kHz)}, \tag{13}$$

where the coefficients a_1 and a_2 (theoretical values[29,34]) are listed in Table 2. (Lines up to 119 GHz are identified by the notation $N^{\pm}$, denoting fine structure transitions between states of total angular momentum $J = N$ and $J = N \pm 1$, where N is the rotational angular momentum quantum number.)

The complex shape function, including first-order effects of line mixing,[25] is

$$\mathbf{F}_k(f) = \frac{f}{\nu_k}\left(\frac{1 - iY_k}{\nu_k - f - i\gamma_k} - \frac{1 + iY_k}{\nu_k + f + i\gamma_k}\right), \tag{14}$$

of which the imaginary part (absorption line profile) is

$$F_k''(f) = \gamma_k(\eta_+ + \eta_-) - Y_k[(\nu_k - f)\eta_+ + (\nu_k + f)\eta_-] \quad \text{(GHz}^{-1}\text{)}, \tag{15}$$

where ν_k is the center frequency, γ_k the half-width, Y_k the mixing parameter, and

$$\eta_\pm = (f/\nu_k)[(\pm\nu_k - f)^2 + \gamma_k^2]^{-1}. \tag{16}$$

The line-broadening parameters in MPM are computed from[28,29]

$$\gamma_k = a_3 \times 10^{-2}[p\theta^{(0.8 - a_4)} + 1.1e\theta] \quad \text{(GHz)}, \tag{17}$$

where the values of ν_k, a_3, and a_4 are tabulated in Table 2. These values are the same as MPM89.[29] In the present case, $e = 0$, and p was replaced by the total pressure P. The mixing parameters Y_k [see Eq. (27) below] were revised in light of the new measurements and they are addressed next.

There was some hint in the measurements that line widths could be greater than the MPM89 values. Residual errors improved slightly (see Table 1) when all widths γ_k were multiplied by the factor 1.05 and simultaneously all mixing parameters Y_k were multiplied by the factor 1.15. However, this result was judged not to be statistically significant (by a 95% F-test). Furthermore, the 100 MHz spacing of the measured frequencies was too sparse to support the extraction of width parameters for individual lines. The width coefficients a_3 are based on earlier measurements[9,28]

Table 2. Spectroscopic parameters of $^{16}O_2$ lines in natural air (MPM92).

Q#	Line Center	Strength		Width		Mixing	
$N\pm$	ν_k	a_1	a_2	a_3	a_4	a_5	a_6
	GHz	10^6×kHz/kPa		10^2×GHz/kPa		10^2 /kPa	
37-	50.474238	0.94	9.694	0.85	0	0.210	0.685
35-	50.987749	2.46	8.694	0.87	0	0.190	0.680
33-	51.503350	6.08	7.744	0.89	0	0.171	0.673
31-	52.021410	14.14	6.844	0.92	0	0.144	0.664
29-	52.542394	31.02	6.004	0.94	0	0.118	0.653
27-	53.066907	64.1	5.224	0.97	0	0.114	0.621
25-	53.595749	124.7	4.484	1.00	0	0.200	0.508
23-	54.130000	228.0	3.814	1.02	0	0.291	0.375
21-	54.671159	391.8	3.194	1.05	0	0.325	0.265
19-	55.221367	631.6	2.624	1.08	0	0.224	0.295
17-	55.783802	953.5	2.119	1.11	0	-0.144	0.613
1+	56.264775	548.9	0.015	1.646	0	0.339	-0.098
15-	56.363389	1344.0	1.660	1.144	0	-0.258	0.655
13-	56.968206	1763.0	1.260	1.181	0	-0.362	0.645
11-	57.612484	2141.0	0.915	1.221	0	-0.533	0.606
9-	58.323877	2386.0	0.626	1.266	0	-0.178	0.044
3+	58.446590	1457.0	0.084	1.449	0	0.650	-0.127
7-	59.164207	2404.0	0.391	1.319	0	-0.628	0.231
5+	59.590983	2112.0	0.212	1.360	0	0.665	-0.078
5-	60.306061	2124.0	0.212	1.382	0	-0.613	0.070
7+	60.434776	2461.0	0.391	1.297	0	0.606	-0.282
9+	61.150560	2504.0	0.626	1.248	0	0.090	-0.058
11+	61.800154	2298.0	0.915	1.207	0	0.496	-0.662
13+	62.411215	1933.0	1.260	1.171	0	0.313	-0.676
3-	62.486260	1517.0	0.083	1.468	0	-0.433	0.084
15+	62.997977	1503.0	1.665	1.139	0	0.208	-0.668
17+	63.568518	1087.0	2.115	1.11	0	0.094	-0.614
19+	64.127767	733.5	2.620	1.08	0	-0.270	-0.289
21+	64.678903	463.5	3.195	1.05	0	-0.366	-0.259
23+	65.224071	274.8	3.815	1.02	0	-0.326	-0.368
25+	65.764772	153.0	4.485	1.00	0	-0.232	-0.500
27+	66.302091	80.09	5.225	0.97	0	-0.146	-0.609
29+	66.836830	39.46	6.005	0.94	0	-0.147	-0.639
31+	67.369598	18.32	6.845	0.92	0	-0.174	-0.647
33+	67.900867	8.01	7.745	0.89	0	-0.198	-0.655
35+	68.431005	3.30	8.695	0.87	0	-0.210	-0.660
37+	68.960311	1.28	9.695	0.85	0	-0.220	-0.665
1-	118.750343	945.0	0.009	1.63	0	-0.031	0.008
	368.498350	67.9	0.049	1.92	0.6	0	0
	424.763124	638.0	0.044	1.926	0.6	0	0
	487.249370	235.0	0.049	1.92	0.6	0	0
	715.393150	99.6	0.145	1.81	0.6	0	0
	773.839675	671.0	0.130	1.81	0.6	0	0
	834.145330	180.0	0.147	1.81	0.6	0	0

with a dispersion spectrometer that was designed for the purpose of making accurate width determinations.

4.2. Fitting of line-mixing coefficients

Line-mixing coefficients were extracted from the absorption at 70.1 kPa pressure, employing Rosenkranz's[25] algorithm with some modifications. To facilitate comparisons between different temperatures, the mixing coefficients are expressed in the normalised form

$$y_k = Y_k \times (10^{-2} P \theta^{0.8})^{-1}. \tag{18}$$

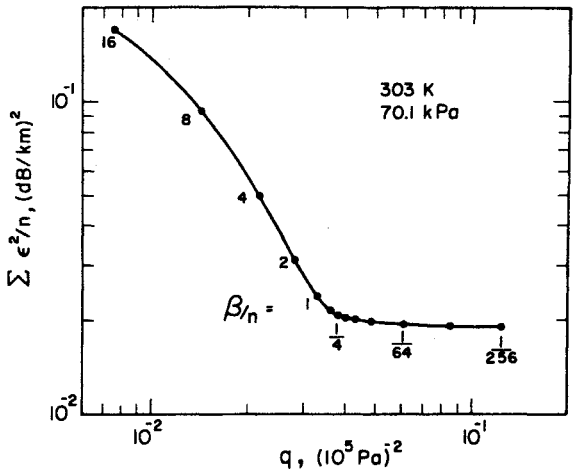

Fig. 3. Imputed error variance for the 70 kPa, 30°C data set vs the cost function q, which is a measure of structure in the intrabranch relaxation matrix, as the parameter β is varied ($n = 192$).

It will be seen, however, that this normalisation does not entirely remove the temperature dependence of y_k. The desired coefficients y_k are related to attenuation rates α_x measured at frequencies f_x by

$$\alpha_x - \alpha_x^b = \Sigma_k W_{xk}(y_k - b_k) + \epsilon_x, \tag{19}$$

where ϵ_x is the (unknown) error in the measurement and α_x^b is absorption† calculated at f_x from Eqs. (10)–(17) by setting $Y_k = b_k P\theta^{0.8}$, with b_k a bias representing the coupling to the nonresonant and antiresonant branches of the oxygen spectrum. The value of the bias is[35]

$$b_k = -0.56 \times 10^{-2}[v_k^{-1} + (v_k + 60)^{-1}] \quad (\text{kPa}^{-1}). \tag{20}$$

For attenuation data, elements of the weight matrix $\mathbf{W}$ are

$$W_{xk} = -0.182 f_x S_k[(v_k - f_x)\eta_+ + (v_k + f_x)\eta_-]10^{-2}P\theta^{0.8}. \tag{21}$$

Calculation of α_x^b and W_{xk} made use of the MPM89 line widths, and the $\eta_\pm$ are given by Eq. (16) where $f = f_x$. Estimated values for the y_k are obtained from the matrix equation

$$y = \mathbf{S}\mathbf{W}^t z + b; \tag{22}$$

here the superscript t denotes transpose, $\mathbf{S} = \mathbf{K}\mathbf{H}^{-1}\mathbf{K}^t$, and the vector

$$z = (\mathbf{W}\mathbf{S}\mathbf{W}^t + \beta\mathbf{I})^{-1}(\boldsymbol{\alpha} - \boldsymbol{\alpha}^b). \tag{23}$$

The quantities α and α^b are vectors containing α_x and α_x^b as elements. The matrix $\mathbf{K}$ relates the vector y to the intrabranch relaxation matrix and $\mathbf{H}$ is the "cost matrix" which specifies the measure of structure in the intrabranch relaxation matrix. Expressions for $\mathbf{K}$, $\mathbf{H}$, and $\mathbf{S}$ are given by Rosenkranz.[25] For a selected value of the scalar parameter β, Eq. (23) minimises $\Sigma_x \epsilon_x^2 + \beta q$, where

$$q = r^t\mathbf{H}r = z^t\mathbf{W}\mathbf{S}\mathbf{W}^t z \tag{24}$$

is the cost function and r is a vector containing the elements of the intrabranch relaxation matrix (normalised in the same way as the y_k). Thus the value of β determines the relative weight that is placed on minimising structure in the relaxation matrix, versus minimising the error in fitting the measurements. Since $\Sigma_x \epsilon_x^2$ increases linearly with the number of measurements n, β should scale with n, other things being equal.

The tradeoff between imputed error and structure, as β is varied, is shown in Fig. 3 for the 70.1 kPa, 30°C data. Similar curves are obtained at other temperatures and pressures. Large values of β emphasise smoothness of the relaxation matrix with corresponding large errors in fitting the

†A fraction of one percent of the total absorption is contributed by the $^{16}O^{18}O$ (0.407%) molecules, whose resonance frequencies differ from $^{16}O_2$. This contribution was included in α^b.

Table 3. Derived y_k-coefficients at three temperatures.

$N^{\pm}$	279 K	303 K	327 K
1-	-0.022	-0.024	-0.024
3-	-0.336	-0.363	-0.348
5-	-0.537	-0.545	-0.548
7-	-0.380	-0.399	-0.416
9-	-0.144	-0.108	-0.153
11-	0.120	0.061	0.025
13-	0.339	0.261	0.238
15-	0.452	0.377	0.350
17-	0.506	0.483	0.408
19-	0.539	0.520	0.492
21-	0.610	0.587	0.568
23-	0.694	0.660	0.635
25-	0.749	0.698	0.669
27-	0.782	0.727	0.684
29-	0.819	0.764	0.716
31-	0.858	0.802	0.753
33-	0.894	0.838	0.788
1+	0.228	0.254	0.242
3+	0.503	0.546	0.522
5+	0.583	0.586	0.595
7+	0.304	0.324	0.349
9+	0.041	0.000	0.053
11+	-0.219	-0.154	-0.115
13+	-0.421	-0.339	-0.316
15+	-0.516	-0.440	-0.412
17+	-0.556	-0.534	-0.458
19+	-0.579	-0.561	-0.534
21+	-0.644	-0.622	-0.603
23+	-0.722	-0.689	-0.664
25+	-0.772	-0.723	-0.694
27+	-0.801	-0.747	-0.705
29+	-0.834	-0.781	-0.733
31+	-0.869	-0.815	-0.767
33+	-0.901	-0.847	-0.798

measurements. Small values of β yield an asymptotically diminishing mean-square error at the expense of rapidly increasing structure in the relaxation matrix. There are more measurements at each pressure and temperature than free parameters y_k; hence the imputed error variance approaches a nonzero value as β decreases. Lacking *a priori* knowledge of the expected value of q, we chose β at the knee of the tradeoff curve. The value $\beta/n = 0.25(10^5\,\text{Pa} \times \text{dB/km})^2$ was

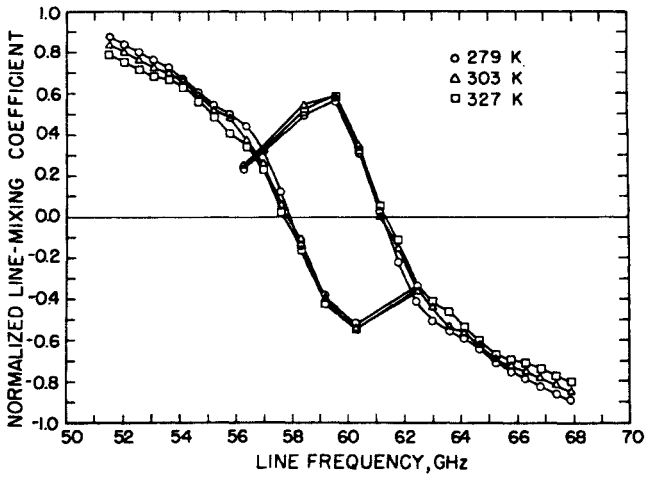

Fig. 4. Normalised mixing coefficients y_k vs line frequency. The normalisation removes the temperature and pressure dependence that is associated with the line widths [see Eq. (18)].

appropriate for all three temperatures at 70 kPa. Diagonalisation of **WSW**[1] showed that four of its eigenvalues exceeded this value of β. Hence there are approximately four degrees of freedom in fitting the y_k to the measurements.

The mixing coefficients y_k thus extracted from the measurements are listed in Table 3, and Fig. 4 plots them vs line frequency. In the lower rotational levels (near the center of the band) the temperature dependence of the mixing parameters is very similar to the line widths. The higher levels have some further variation with temperature; this can be understood in relation to the detailed balancing constraint on the imaginary part $\mathbf{M}''$ of the relaxation matrix [Ref. 40, Eq. (41)]

$$M''_{jk} = M''_{kj} \exp[(E_k - E_j)/kT], \tag{25}$$

where E_k is the initial energy level of a line with the index k. The diagonal elements M''_{kk} are equal to the line-halfwidth γ_k, while the off-diagonal elements define Y_k, which to first order in $\mathbf{M}''$ is[22]

$$Y_k = (2/\mu_k) \sum_{j \neq k} \mu_j M''_{jk} (\nu_k - \nu_j)^{-1}, \tag{26}$$

where the μ_k are reduced dipole matrix elements as defined by Edmonds.[41] The elements of $\mathbf{M}''$ close to the main diagonal tend to be largest. The rotational constant of O_2 is 43.1 GHz, so the sum in Eq. (26) for Y_k is dominated by terms in which k and j correspond to levels that are not widely separated compared to kT. By approximating the exponential in Eq. (25) as $1 + (E_k - E_j)/kT$, one can see that if the temperature variation in the Ys contains a term that varies with θ^x, then for at least some of the coefficients there will also be a term varying with $\theta^{(x+1)}$. This argument does not prove that two terms in powers of θ will always be sufficient to represent the temperature dependence of the Y_k, but at least two are necessary to maintain detailed balance.

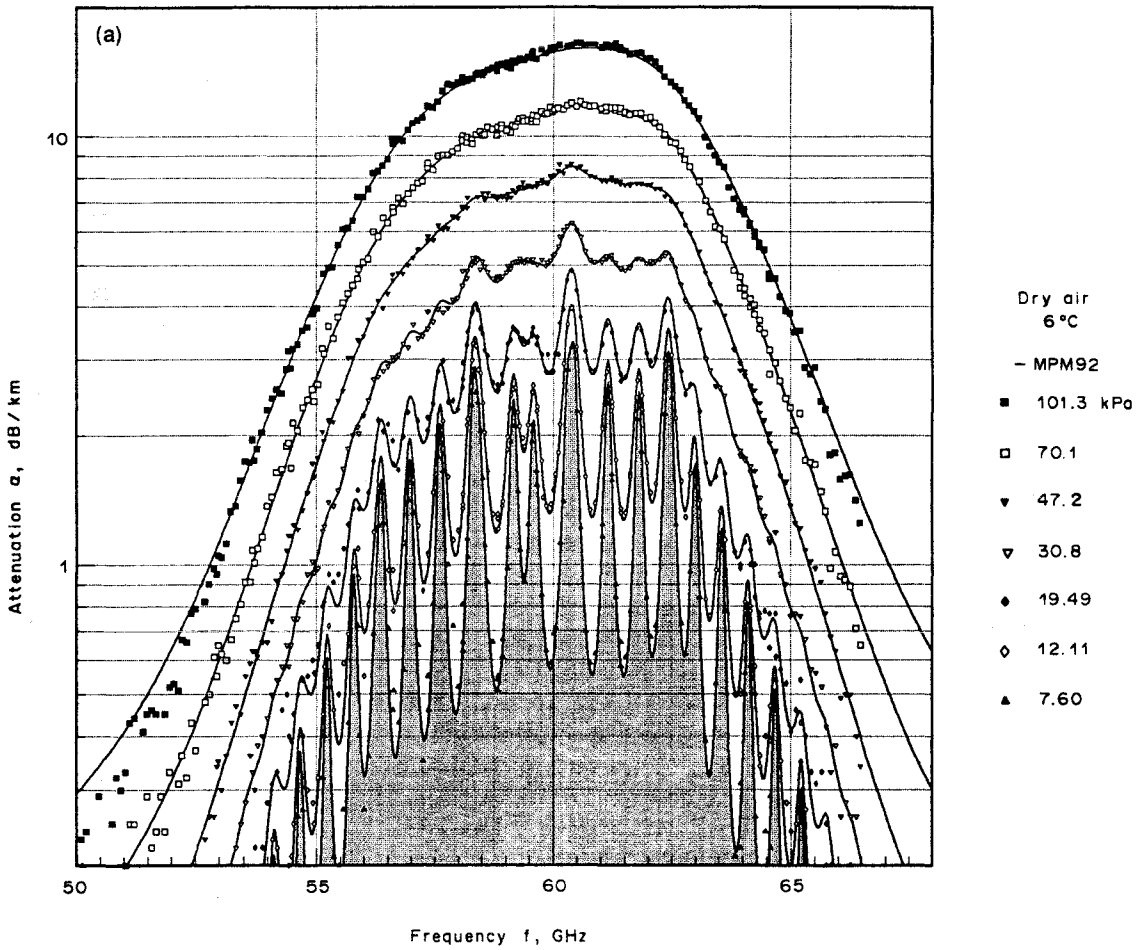

Fig. 5a—*Caption on page 641*

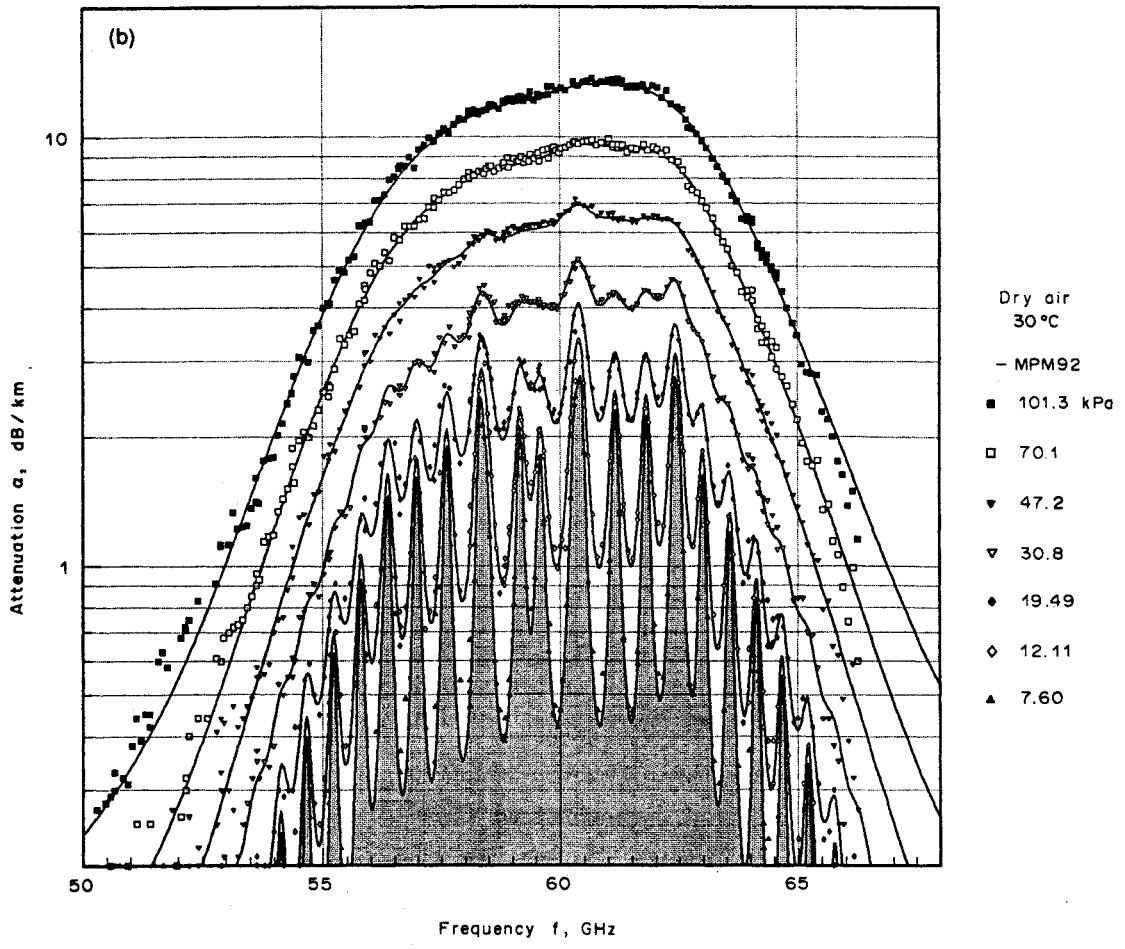

Fig. 5b—*Caption on page 641*

In the MPM the temperature and pressure dependence of the line mixing parameters is

$$Y_k = (a_5 + a_6\theta)10^{-2}P\theta^{0.8}. \tag{27}$$

The coefficients a_5 and a_6, which are listed for each line in Table 2, were derived from the y_k in Table 3 by an ordinary least-squares fit to the three temperatures. The measurements at pressures other than 70 kPa were not used to determine coefficients in the model. These data provide a test of the pressure dependence of absorption predicted by the MPM. The comparisons are shown in Figs. 5(a, b, c) and 6. (The 70 kPa data used to derive the mixing coefficients are also plotted.) The r.m.s. residuals for all measured pressures and temperatures are plotted in Fig. 2.

In general, MPM92 fits the data well. In Fig. 5 the calculations are indistinguishable from the results that would be obtained by using the y_k fitted to each temperature separately. Thus the two-term expansion in θ, Eq. (27), seems to be adequate for the 48 K range that was covered in this series of measurements. A magnitude of unity for the Y-parameters is a rough upper limit to the validity of a first-order expansion in gas density (or pressure), and the largest of the Y_k approach this value at 101 kPa. At this pressure, some small departures from the first-order expansion can be seen. For example, in Fig. 6 at 61 GHz, the centroid of the 6°C-measurements is approximately 16.2 dB/km, while MPM predicts 16.0 dB/km. (For comparison, 13.3 dB/km results if a_5 and a_6 are set equal to zero.)

Fitting the mixing coefficients to 47 kPa data produced virtually the same results as in Table 3, but the magnitude of the line-mixing effect becomes smaller at lower pressures. Hence, 70 kPa seems to be a good compromise, at least for this data set, between maximising the signal-to-noise ratio and avoiding errors due to omitted higher-order line mixing. The second-order terms of an expansion in gas pressure (see Ref. 24) change the line intensities and resonant frequencies, and

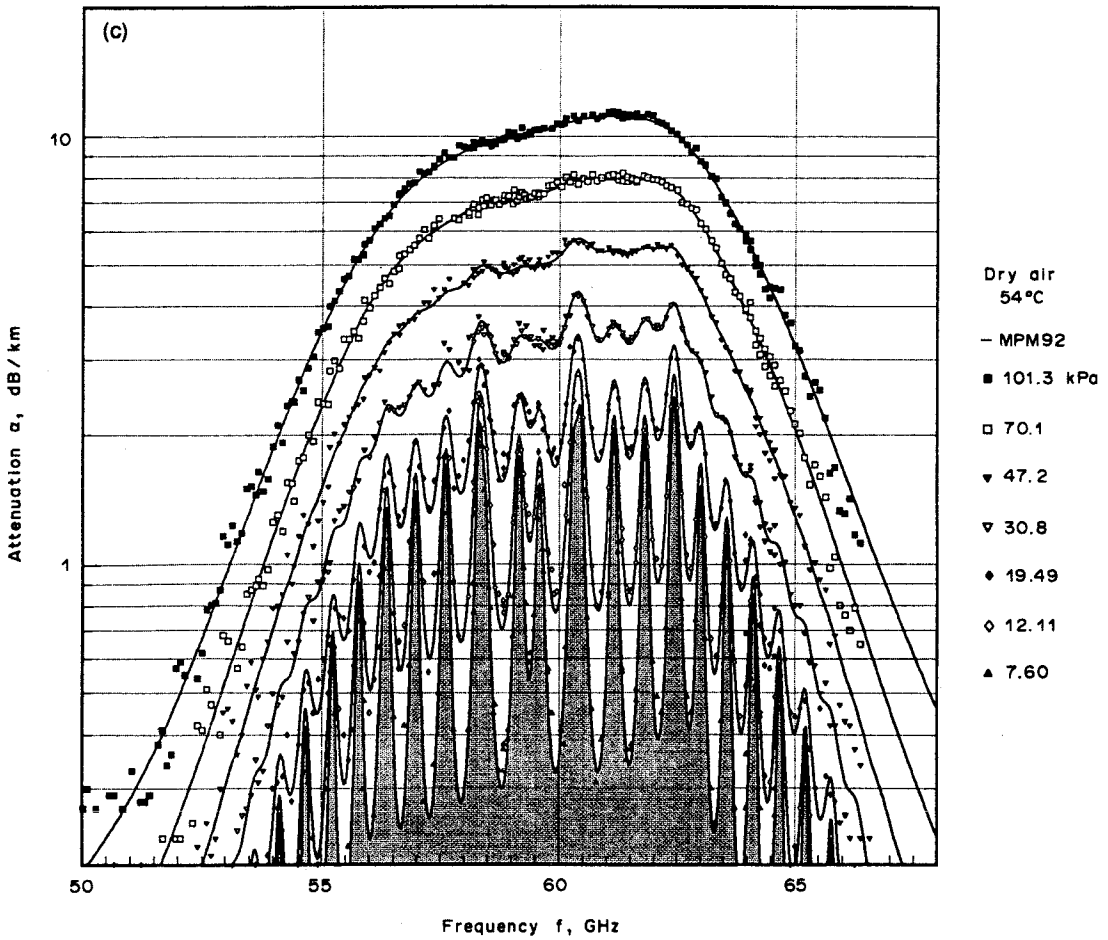

Fig. 5. Attenuation measurements of *test air* between 50 and 68 GHz at seven pressures from 7.6 to 101.3 kPa. The curves are computed from MPM92: (a) $T = 6°C$ (279 K), (b) $T = 30°C$ (303 K), and (c) $T = 54°C$ (327 K).

thus have the effect of redistributing absorption within the 50–70 GHz band. The first-order terms have that effect, but also redistribute absorption from the distant wings into the center of the band. The MPM should be accurate at 1 atm pressure in the atmospheric "windows" centered near 35, 90, and 140 GHz.[31]

The normalised mixing coefficients for 303 K, plotted in Fig. 4, can be compared with line mixing coefficients derived by Rosenkranz[25] from the earlier dispersion-spectrometer measurements. (One could also take $a_5 + a_6$, which is exactly equal to Y at 300 K and 100 kPa.) The new mixing coefficients have a roughly similar variation with rotational quantum number N, but the low-N peaks near 60 GHz are 12% smaller and the high-N coefficients are larger. The new Y-coefficients are believed to be more accurate, especially their temperature dependence, by virtue of being based on a much larger data set (190 × 3 α-measurements between 279 and 327 K vs 41 N'-data[14] taken only at 300 K), but the recognised differences might be taken as an upper limit on their uncertainty (given the line widths as fixed). However, in both cases the coefficients for the weak lines below 54 GHz and above 65 GHz are determined primarily by the constraints in the retrieval algorithm rather than by the data.

Finally, it may be useful to review the limitations of the method by which coefficients a_5 and a_6 have been derived: (i) they pertain to a first-order expansion [Eq. (27)] in pressure. It is possible to approximate the oxygen-band shape to higher order[24], but an algorithm for extracting the additional coefficients from measurements has not been developed. In view of the smallness of systematic residual discrepancies in Figs. 5 and 6 relative to the scatter of the data, an attempt to derive higher-order coefficients might be futile. (ii) There is no coupling between the two branches of the O_2-band in the present algorithm, and the intrabranch relaxation matrices are assumed to

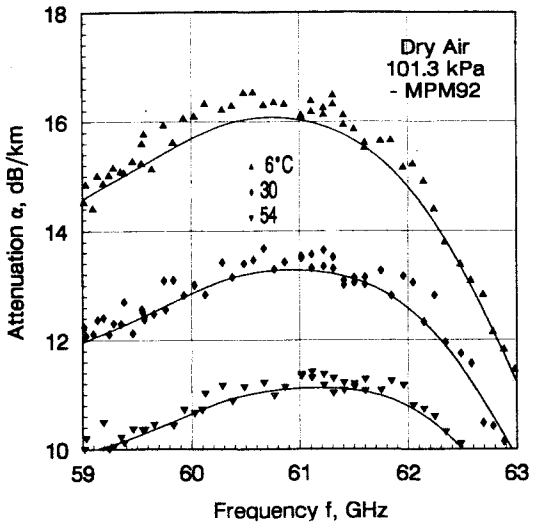

Fig. 6. Attenuation measurements of *test air* at 101.3 kPa for three temperatures (6, 30, and 54°C) expanded in frequency from 59 to 63 GHz (see Fig. 5).

be identical. It is possible that to some extent these approximations eliminate degrees of freedom in the coefficients that would be useful in fitting the measurements more closely. (iii) The two-term expansion in θ, though adequate to fit the present set of measurements, might fail outside the temperature range investigated here.

5. CONCLUSIONS AND RECOMMENDATIONS

Collisional broadening causes the lines of the atmospheric 60-GHz oxygen spectrum to overlap at pressures above 10 kPa. Experimental results were applied to improve predictions of attenuation rates. A reliable model is particularly valuable to atmospheric radiative transfer problems.[34] Experimental principles, instrumental performance, examples of spectroscopic results, and the measurement uncertainties have been discussed. Measurements were performed at frequencies between 49.3 and 66.3 GHz in 100 MHz steps at three temperatures (6, 30, 54°C) for 11 selected pressure values.

The extensive data set improves the molecular data base for the atmospheric 60-GHz oxygen spectrum. The results obtained from this investigation of line mixing in the oxygen microwave band can contribute, in conjunction with theoretical calculations, to the determination of inelastic transition rates in molecular collisions. Each mixing parameter Y_k is related by Eq. (26) to a sum in which typically a small number of terms in the off-diagonal elements of **M** predominate. Theoretical calculations of these parameters would provide a stringent test for models of the intermolecular potential.

Additional experimental work on the atmospheric 60-GHz O_2 spectrum is suggested in four areas: (a) analyze the refractivity data, Re **N** [Eq. (6)], which were taken simultaneously with the attenuation rates; (b) continue measurement series at subfreezing temperatures (0 to −50°C) to simulate real atmospheric conditions; (c) measure the pressure-broadened widths of individual lines with a finer frequency grid (10–1 MHz) for pressures in the 0.5–5 kPa range, and (d) study the Zeeman effect of O_2 lines with very high frequency resolution (10–0.01 MHz) under controlled geomagnetic field simulations.

Acknowledgements—The authors thank D. H. Staelin for comments on the manuscript and M. G. Cotton for assistance with computations. The work of one of us (P.W.R.) was supported under an agreement with S. M. Systems and Research Corp.

REFERENCES

1. J. H. VanVleck, *Phys. Rev.* **71,** 413 (1947).
2. R. M. Hill and W. Gordy, *Phys. Rev.* **93,** 1019 (1954); J. O. Artman and H. P. Gordon, *ibid.* **96,** 1237 (1954).

3. L. G. Stafford and C. W. Tolbert, *J. Geophys. Res.* **68,** 3441 (1963).
4. E. E. Reber, *J. Geophys. Res.* **77,** 3831 (1972).
5. J. W. Waters, *Nature* **242,** 506 (1973).
6. L. R. Zink and M. Mizushima, *J. Molec. Spectrosc.* **125,** 154 (1987).
7. W. C. Gardiner Jr., H. M. Pickett, and M. H. Proffitt, *J. Chem. Phys.* **63,** 2149 (1975); *ibid.* **74,** 6037 (1981); B. J. Setzer and H. M. Pickett, *ibid.* **67,** 340 (1977); R. G. Utter and W. C. Gardiner Jr., *ibid.* **91,** 2054 (1989).
8. H. M. Pickett, E. A. Cohen, and D. E. Brinza, *Astrophys. J.* **258,** L49 (1981).
9. H. J. Liebe, G. G. Gimmestad, and J. D. Hopponen, *IEEE Trans. Antennas Propag.* **AP-25,** 327 (1977); *Proc. Int. Sym. URSI-F,* p. 619, LaBaule, France (May 1977).
10. W. G. Read, K. W. Hillig II, E. A. Cohen, and H. M. Pickett, *IEEE Trans. Antennas Propag.* **AP-36,** 1136 (1988).
11. A. A. Vlasov, V. V. Glyzin, E. N. Kadygrov, and E. A. Kuklin, *Izv. Acad. Sci. U.S.S.R., Atm. Ocean. Phys.* **26,** 734 (1990).
12. H. J. Liebe, G. A. Hufford, and R. O. DeBolt, "The Atmospheric 60-GHz Oxygen spectrum: Modeling and Laboratory Measurements," NTIA-Report 91–272; U.S. Dept. Commerce, Boulder, CO; NTIS Order No. PB 91-172809 (1991).
13. H. J. Liebe, *Rev. Sci. Instrum.* **46,** 817 (1975).
14. H. J. Liebe and D. A. Layton, "Millimeter-wave Properties of the Atmosphere," NTIA Report 87-224; U.S. Dept. Commerce, Boulder, CO; NTIS Order No. PB 88-164215/AF (1987).
15. S. A. Zhevakin and A. P. Naumov, *Radio Engng Electron. Phys.* **10,** 987 (1965).
16. R. G. Gordon, *J. Chem. Phys.* **46,** 448 (1967).
17. U. Mingelgrin, *Molec. Phys.* **28,** 1591 (1974).
18. T. A. Dillon and J. T. Godfrey, *Phys. Rev.* **A5,** 599 (1972).
19. E. W. Smith and M. Guiraud, *J. Chem. Phys.* **71,** 4209 (1979); *errata* **74,** 355 (1981).
20. R. A. Poynter and H. M. Pickett, *Appl. Opt.* **24,** 2235 (1985).
21. R. J. Hill, *IEEE Trans. Antennas Propag.* **AP-35,** 198 (1987).
22. P. W. Rosenkranz, *IEEE Trans. Antennas Propag.* **AP-23,** 498 (1975).
23. K. S. Lam, *JQSRT* **17,** 351 (1977).
24. E. W. Smith, *J. Chem. Phys.* **74,** 6658 (1981).
25. P. W. Rosenkranz, *JQSRT* **39,** 287 (1988).
26. W. B. Lenoir, *J. Geophys. Res.* **68,** 1683 (1963).
27. G. A. Hufford and H. J. Liebe, "Millimeter-wave Propagation in the Mesosphere," NTIA-Report 89-249; U.S. Dept. Commerce, Boulder, CO; NTIS Order No. PB 90-119868/AS (1989).
28. H. J. Liebe, *Radio Sci.* **16,** 1183 (1981); *ibid.* **20,** 1069 (1985).
29. H. J. Liebe, *Int. J. Infrared Mill. Waves* **10,** 631 (1989).
30. G. M. Brussard, E. Damosso, and L. Stola, *CSELT Rapp. Tech.* **XI,** 313 (1983).
31. H. J. Liebe, *IEEE Trans. Antennas Propag.* **AP-31,** 127 (1983).
32. M. L. Meeks and A. E. Lilley, *J. Geophys. Res.* **68,** 1683 (1963).
33. N. C. Grody, *J. Clim. Appl. Met.* **22,** 609 (1983).
34. P. W. Rosenkranz, Chap. 2 in *Atmospheric Remote Sensing by Microwave Radiometry,* M. A. Janssen ed., Wiley, New York, N.Y. (1992).
35. H. J. Liebe, V. L. Wolfe, and D. A. Howe, *Rev. Sci. Instrum.* **55,** 1702 (1984).
36. H. Kugelnik and T. Li, *Proc. IEEE* **54,** 1312 (1966).
37. G. Schulten, *Frequencz* **20,** 10 (1966).
38. L. Machta and E. Hughes, *Science* **168,** 1582 (1970).
39. D. W. Marquardt, *J. Soc. Indust. Appl. Math.* **11,** 431 (1963).
40. A. Ben-Reuven, *Phys. Rev.* **145,** 7 (1966).
41. A. R. Edmonds, *Angular Momentum in Quantum Mechanics,* Princeton Univ. Press, Princeton, N.J. (1974).